ACS NANO

www.acsnano.org

ARTICLE

Enhanced Nanobubble Formation: Gold Nanoparticle Conjugation to Qβ Virus-like Particles

Perouza Parsamian, Yaning Liu, Chen Xie, Zhuo Chen, Peiyuan Kang, Yalini H. Wijesundara, Noora M. Al-Kharji, Ryanne Nicole Ehrman, Orikeda Trashi, Jaona Randrianalisoa, Xiangyu Zhu, Matthew D'Souza, Lucas Anderson Wilson, Moon J. Kim, Zhenpeng Qin,* and Jeremiah J. Gassensmith*

Cite This: https://doi.org/10.1021/acsnano.3c00638

Read Online

ACCESS | Metrics & More | Article Recommendations | Supporting Information

ABSTRACT: **Plasmonic gold nanostructures are a prevalent tool in modern hypersensitive analytical techniques such as photoablation, bioimaging, and biosensing. Recent studies have shown that gold nanostructures generate transient nanobubbles through localized heating and have been found in various biomedical applications. However, the current method of plasmonic nanoparticle cavitation events has several disadvantages, specifically including small metal nanostructures (≤10 nm) which lack size control, tuneability, and tissue localization by use of ultrashort pulses (ns, ps) and high-energy lasers which can result in tissue and cellular damage. This research investigates a method to immobilize sub-10 nm AuNPs (3.5 and 5 nm) onto a chemically modified thiol-rich surface of Qβ virus-like particles. These findings demonstrate that the multivalent display of sub-10 nm gold nanoparticles (AuNPs) caused a profound and disproportionate increase in photocavitation by upward of 5−7-fold and significantly lowered the laser fluency by 4-fold when compared to individual sub-10 nm AuNPs. Furthermore, computational modeling showed that the cooling time of QβAuNP scaffolds is significantly extended than that of individual AuNPs, proving greater control of laser fluency and nanobubble generation as seen in the experimental data. Ultimately, these findings showed how QβAuNP composites are more effective at nanobubble generation than current methods of plasmonic nanoparticle cavitation.**

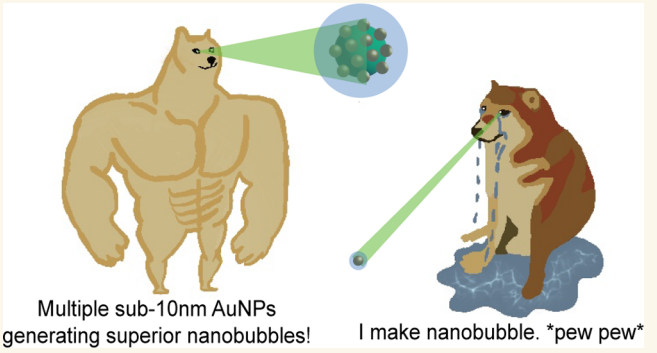

KEYWORDS: *plasmonic gold nanoparticles, virus-like particles, plasmonic nanobubble, transient heating, photothermal*

INTRODUCTION

Plasmonic gold nanostructures are among the most well-known and oldest nanotechnologies and can be found in applications from modern hypersensitive analytical techniques to ancient art.[1] The contemporary utility of gold nanostructures is owed to their straightforward synthesis and tunable intense color, which arises from a photoinduced oscillation of surface electrons creating the plasmon.[2−5] These plasmonic nanostructures can be designed to efficiently convert incident laser energy into heat, known as the photothermal effect, and have found wide applications in photothermal therapies and point-of-care diagnostics.[6−8] One of the potential responses to the photothermal effect is nanobubble generation. By tuning the topology of the nanostructure and the heating duration, transient nanobubble cavitation and collapse can be observed, which creates significant shear forces capable of temporarily or permanently altering vasculature.[9−11]

These shear forces, which arise from the rapid cavitation of the nanobubble, are powerful enough to remodel tissue. This has given them utility in nanosurgical applications; for instance, recent work has found that plasmonically induced cavitation events can create temporary openings in the blood−brain barrier.[12,13] With state-of-the-art methodologies using

Received: January 20, 2023
Accepted: March 6, 2023

small metal nanostructures (<10 nm), effective methods of plasmonic nanostructure cavitation lack size control, tuneability, and tissue localization.[14−19] An articulated drawback to utilizing these metal nanostructures is that they require ultrashort pulsed lasers and high laser energy, which can induce unwanted tissue damage.[20−27] Thus, finding new architectures and composites of gold that can reduce the laser flux can help spare healthy tissue and reduce the amount of gold needed for a therapeutic effect. This cavitation effect has been enhanced upon aggregation of gold nanoparticles (AuNPs), albeit with larger nanoparticles. For instance, intracellular clustering of AuNPs has been shown to induce greater vapor nanobubble generation, enabling mechanical disruptions of the cell membrane via direct AuNP therapies.[28] Other studies also combined chemotherapy with plasmonic nanobubbles (PNBs) to achieve efficient thermal destruction of cancer cells by taking advantage of the formation of NP clusters, showing promise for *in vivo* nanoparticle-based photothermal therapies.[22,24,29]

Herein, we show the colocalization of many sub-10 nm AuNPs via immobilization onto a virus-like particle (VLP) as a superior alternative to individual sub-10 nm AuNPs (Scheme 1). VLPs are non-infectious engineered biodegradable

Scheme 1. A Schematic Illustration of Plasmonic Nanobubble Signal Generation Comparing sub-10 nm AuNPs Immobilized onto VLP Scaffolds vs Individual sub-10 nm AuNPs

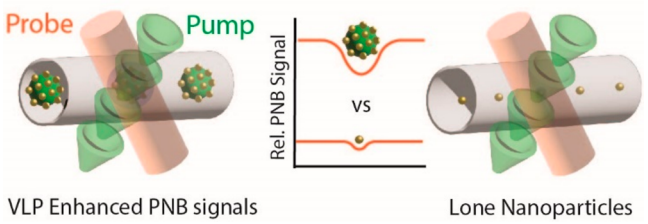

nanostructures derived from viral proteins. The structure of most VLPs is known to atomistic detail, and their exposed surfaces can be functionalized using high-yielding bioconjugation chemistry. In particular, VLP Qβ—the crystal structure displayed in Figure 1A—has been used extensively as a proteinaceous nanocarrier, as its well-understood surface chemistry, minimal toxicity, and low reactogenicity have made it an ideal biodegradable delivery platform.[30] Qβ is an icosahedral VLP comprised of 180 coat proteins connected through disulfide bonds (Figure 1A yellow residues) with four solvent-exposed primary amine residues from lysine (Figure 1A green residues), which have been chemically modified for use in multiple biomedical applications, including contrast agents, photothermal scaffolds, and drug carriers.[31−48]

In this work, we detail a method to immobilize either 3.5 or 5 nm AuNPs onto a chemically modified thiol-rich surface of Qβ. We found that the multivalent display of approximately 46 sub-10 nm AuNPs induces a significant increase in the photocavitation efficiency by 5-fold compared to traditional sub-10 nm AuNPs. Computational modeling shows that the absorption cross-section (C_{abs}) for the QβAuNP conjugation is higher than that of the single AuNP heating due to the plasmonic coupling. Notably, the heating overlap leads to a significantly higher maximum temperature rise in water and longer cooling time versus single AuNP heating, which may

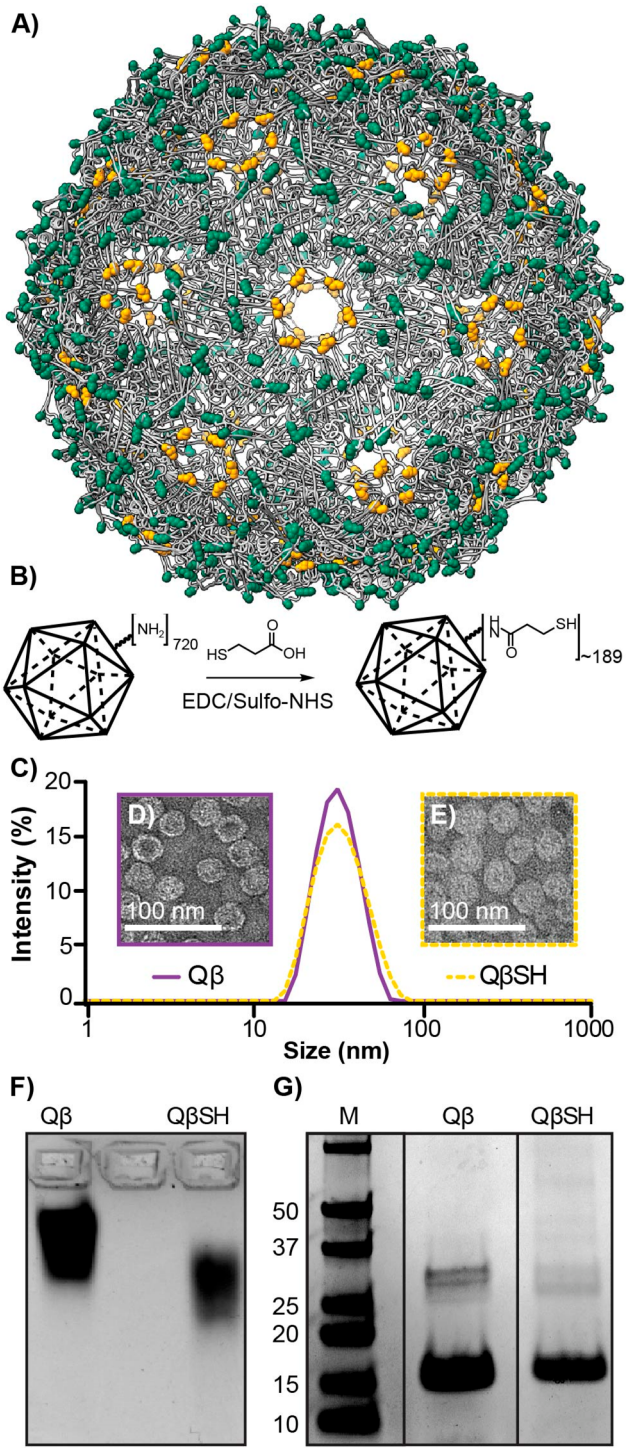

Figure 1. (A) Qβ, an icosahedral VLP, is composed of 180 coat proteins connected through disulfide bonds (yellow). In addition, each coat protein has four solvent-exposed primary amine residues (green) available for bioconjugation. (B) A scheme illustrating Qβ surface functionalization of MPA through EDC/sulfo-NHS coupling. (C) DLS of Qβ (purple) and QβSH (yellow-dashed). (D) TEM of Qβ (purple) and (E) QβSH (yellow-dashed). (F) Coomassie-stained 1% agarose gel of Qβ (left) and QβSH (right) and (G) 10% SDS-PAGE gel of Qβ (left) and QβSH (right).

account for the increased nanobubble signal.[49] The plasmonic and heat coupling contributes to the significant increase in photocavitation efficiency.

https://doi.org/10.1021/acsnano.3c00638
ACS Nano XXXX, XXX, XXX−XXX

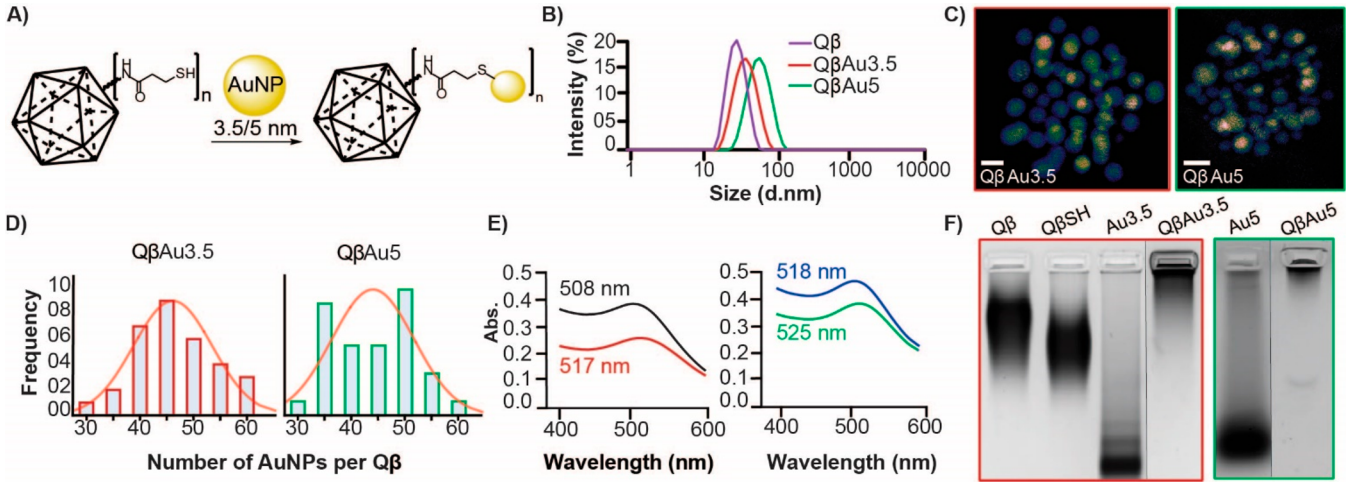

Figure 2. (A) A scheme illustrating 3.5 and 5 nm AuNPs immobilization onto the surface of QβSH. (B) DLS of Qβ and QβAuNPs. (C) STEM micrographs of immobilized AuNPs onto the surface of QβSH. Scale bar: 5 nm. (D) Distribution frequency of immobilized AuNPs to functionalized Qβ thiol: Au3.5 (left) and Au5 (Right) (n = 32 per size). (E) UV-vis spectra show a redshift of Au3.5 (black) and Au5 (blue) to immobilized QβAuNPs (QβAu3.5 (red) and QβAu5 (green)). (F) Coomassie-stained 1% agarose gel of Qβ, QβSH, AuNPs, and QβAuNPs.

RESULTS AND DISCUSSION

QβAuNP Synthesis and Conjugation. The synthesis of the polyvalent VLP-gold nanosystem began with the functionalization of the solvent-exposed amine residues of Qβ with 3-mercaptopropionic acid (MPA). MPA was conjugated in a single set via EDC/sulfo-NHS coupling under mildly acidic conditions to yield the thiolated VLP QβSH (Figure 1B). The successful thiolation of Qβ was determined by electrophoretic mobility assays, and the retention of the spherical morphology was confirmed through dynamic light scattering (DLS) and transmission electron microscopy (TEM). As depicted in Figure 1C, DLS showed almost no change in hydrodynamic radius between Qβ (Z-average: 31.09 ± 1.00 d. nm) and the thiolated Qβ (QβSH) (Z-average: 31.49 ± 0.27 d. nm). As expected, TEM micrographs confirmed no changes to the size or morphology between Qβ (Figure 1D) and QβSH (Figure 1E). Conjugation was confirmed by electrophoretic mobility through 1% agarose gel (Figure 1F), which showed a significant shift for QβSH toward the positive electrode. This shift is anticipated as a result of converting the positively charged lysines into thiol-terminated amides. The colorimetric thiol-selective Ellman's assay was used to quantify free thiols and revealed that approximately 189 ± 0.0106 thiols were conjugated onto the surface of Qβ. Lastly, 10% SDS-PAGE (Figure 1G) shows monomer (14.25 kDa) and dimer coat proteins running approximately the same distance, which is anticipated based on the very low MW (106 Da) of the MPA. From these results, we conclude that QβSH remains intact and possesses approximately one free thiol per coat protein.

Following successful bioconjugation to create a thiol-rich Qβ, we turned to immobilize AuNPs onto the viral surface.

We chose to use 3.5 and 5 nm AuNPs, to study differences in their ability to attach to the surface of QβSH and assess the photothermal responses of two variably sized plasmonic AuNPs. Attachment of AuNPs to Qβ was done in Milli-Q Ultrapure water at a pH of 7 at room temperature (rt) for 12–15 h Figure 2A. As shown in Figure 2B, DLS shows an expected increase in hydrodynamic radius. Both composites 3.5 nm (Z-average 40.03 ± 0.17 d. nm) and 5 nm (Z-average: 67.48 ± 4.69 d. nm) exhibit an increase in size, with the larger 5 nm gold creating a larger composite nanoparticle. These size distributions of the QβAuNP composites were assessed by scanning transmission electron microscopy (STEM) high-angle annular dark-field imaging, and the results are shown in Figure 2C.

To further understand how much gold was attached to each virus, we investigated the number of AuNP immobilized onto Qβ. A histogram was produced from visual analysis of STEM micrographs, and individual AuNPs were counted on QβSH VLPs. Each scaffold showed an average of 46 individual AuNPs per surface-functionalized QβSH (Figure 2D) (n = 32). The apparent difference in distribution is likely a result of experimental variation. STEM imaging allows us to visualize the boundaries of overlapping gold nanostructures, which helps make it clear that the AuNPs are evenly distributed on the surface of the VLP and have not aggregated nor changed diameter. Wide-field imaging (Figure S2H) with TEM shows little to no unconjugated AuNPs in solution, agreeing with our electrophoretic mobility assay. Interestingly, UV-vis spectroscopic analysis shows a significant redshift of the free AuNPs when bound to Qβ (Figure 2E). Since the AuNP diameters are unchanged per STEM imaging, we suspect this shift results from the plasmonic coupling between close AuNPs. When attached to the virus, the smaller gold nanostructures have a slightly larger bathochromic shift (9 nm vs 7 nm). Electrophoretic analysis on 1% agarose shows no free Qβ or QβSH, which suggests that all the QβSH has been functionalized with AuNPs (Figure 2F).

Nanobubble Generation and Detection. Next, we investigated the photothermal affects of conjugated QβAuNP complex versus individual AuNPs, by activating and detecting the PNB. PNBs are formed when the pulsed pump laser beam activates the AuNP-based samples flowing through the microscale detection zone. The confined heating within this zone causes localized evaporation of the media surrounding the AuNPs, creating the PNBs. The resulting PNBs optically scatter light and can be synchronically detected by a continuous probe laser (Figure 3A). Since the PNBs are transient events with submicrosecond lifetimes, we set the

https://doi.org/10.1021/acsnano.3c00638
ACS Nano XXXX, XXX, XXX–XXX

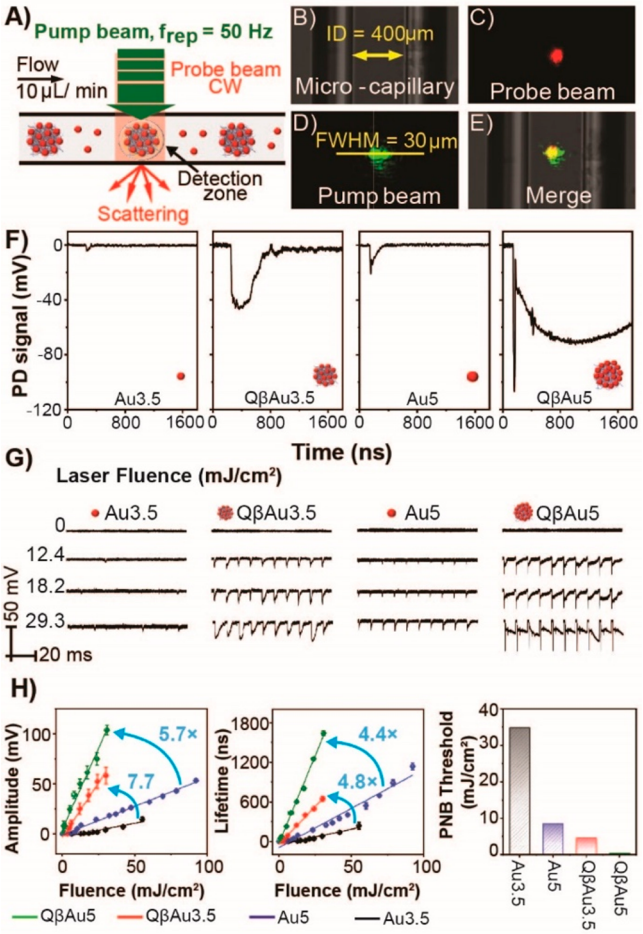

Figure 3. PNB detection for individual AuNPs and conjugated QβAuNPs. A) Schematic illustration of PNB detection. (B) Bright-field images of 400 μm borosilicate glass microcapillary, (C) 633 nm probe laser beam, (D) 532 nm pump laser beam, where the beam diameter is calculated based on the full width half-maximum (fwhm) of the intensity profile of the Gaussian pump beam, and (E) two aligned laser beams merged inside the microcapillary. (F) Typical PNB signals generated by Au3.5, QβAu3.5, Au5, and QβAu5 with the same optical density (O.D. = 0.4) at the laser fluence = 29.3 mJ/cm². (G) Representative PNB signal traces (10 pulses) collected for samples from Au3.5, QβAu3.5, Au5, and QβAu5, respectively. PNB signals analysis by (H) amplitude, (I) lifetime, and (J) energy threshold was plotted for small AuNPs and conjugated QβAuNPs upon different laser fluence heating.

pump laser with a repetition rate of 50 Hz and sample flow speed of 10 μL/min, avoiding repeated heating and detection of the same PNB event. Inside a microcapillary (Figure 3B), two colocalized laser beams—a probe laser beam (Figure 3C) and a pump laser beam (Figure 3D)—are aligned together (Figure 3E) to create a virtual detection zone. We first tested individual AuNPs and QβAuNPs of different sizes at a high laser fluence (29.3 mJ/cm²) to observe PNB signals for all samples. In particular, we tested 3.5 nm AuNPs (Au3.5), Qβ with 3.5 nm AuNPs attached to the surface (QβAu3.5), 5 nm AuNPs (Au5), and Qβ with 5 nm AuNPs attached to the surface (QβAu5). All samples were prepared at the same optical densities (O.D. = 0.4), ensuring equivalent optical absorption for PNB testing. Among those tested samples (Figure 3F), both QβAu3.5 and QβAu5 conjugates result in increased signals corresponding to the larger PNBs generated as compared to individual particles: Au3.5 and Au5, respectively. On the other hand, when we slightly alter the size of AuNPs on Qβ (i.e., from 3.5 to 5 nm), QβAu5 further enhances PNB signals dramatically. To fully investigate their thermal responses, we examined the PNB generation for each case under various laser fluences. Figure 3G depicts representative PNB signal traces (10 pulses) collected for Au3.5, QβAu3.5, Au5, and QβAu5, respectively, and shows laser energy-dependent PNB signals.[50] At no laser or low laser fluence conditions, no PNB signal was detected, whereas higher laser fluence leads to larger PNB signals. Compared with small Au3.5 and Au5, large Au aggregates (i.e., QβAu3.5 and QβAu5) tend to produce PNBs much easier. To understand this phenomenon, we analyzed the PNB signals by their unique amplitudes (Figure 3H), lifetimes (Figure 3I), and generation threshold (Figure 3J). We found linear correlations between the amplitude and lifetime of PNB signals versus the laser fluence for all the tested samples. We compared the slopes of the amplitude and lifetime plots for Au3.5, Au5, QβAu3.5, and QβAu5. Notably, QβAu3.5 and QβAu5 conjugates have slopes of amplitudes that are 7.7- and 5.7-times higher than the Au3.5 and Au5, respectively. Similar trends are exhibited in the lifetime plot, where QβAu3.5 and QβAu5 conjugates have slopes that are 4.8- and 4.4-times higher than the Au3.5 and Au5, respectively. QβAu5 impressively doubled the slope of QβAu3.5, indicating its long bubble-breaking time because of the larger bubble size. Lastly, we explored the PNB generation threshold for each sample (Figure S3). Here the PNB generation threshold (F_{thresh}) was defined at the laser fluence with 50% PNB probability, which describes the minimal amount of laser fluence required to expand the vapor bubble around AuNPs. In the probability plot, Au3.5 and Au5 require high laser fluence to create the PNBs (F_{thresh} = 34.7 and 8.5 mJ/cm²). QβAu3.5, considered a cluster of Au3.5, dramatically lowered the PNBs threshold to 4.5 mJ/cm². Furthermore, increasing the size of AuNP conjugated onto Qβ lowers the PNB generation threshold, thus tuning the thermal responses. For example, QβAu5 possesses a mild PNB generation threshold of 0.45 mJ/cm², which works for non-invasive *in vivo* studies using laser treatment while maintaining tissue integrity.[51,52] Together, QβAu5 exhibits superior thermal responses over all tested samples owing to its highest PNB amplitude, lifetime, and lowest PNB generation threshold.

Nanothermal Transport of Conjugated QβAuNPs. Lastly, we investigated the plasmonic and heat coupling of QβAuNPs by numerical simulations. We first determined the plasmonic and heating response for the QβAuNPs composites with a 3D-FEM simulation model (Figure 4A). Figure 4B–E shows the near-field enhancement ($(E/E_0)^2$) profile with λ = 532 nm and temperature rise (ΔT) profiles (t = 26 ps, 35 ps) for QβAuNP conjugation and individual AuNP, respectively. As illustrated in the $(E/E_0)^2$ profiles, for both QβAu5 and QβAu3.5, the plasmonic coupling is minimal and can only lead to a slight increase in the absorption cross-section (C_{abs}) compared with that of the single AuNP (Figure 4F and Table S1). In contrast, as shown in Figure 4B–E, despite limited heating overlap at the end of the laser pulse (t_1 = 26 ps), further heat dissipation after the laser pulse (t_2 = 35 ps) leads to significant heating overlap, leading to collective heating between the AuNPs. We further analyzed this heating process with the temporal evolution of ΔT at representative locations. Figure S4 shows that, under laser radiation (34.8 mJ/cm²), the

https://doi.org/10.1021/acsnano.3c00638
ACS Nano XXXX, XXX, XXX−XXX

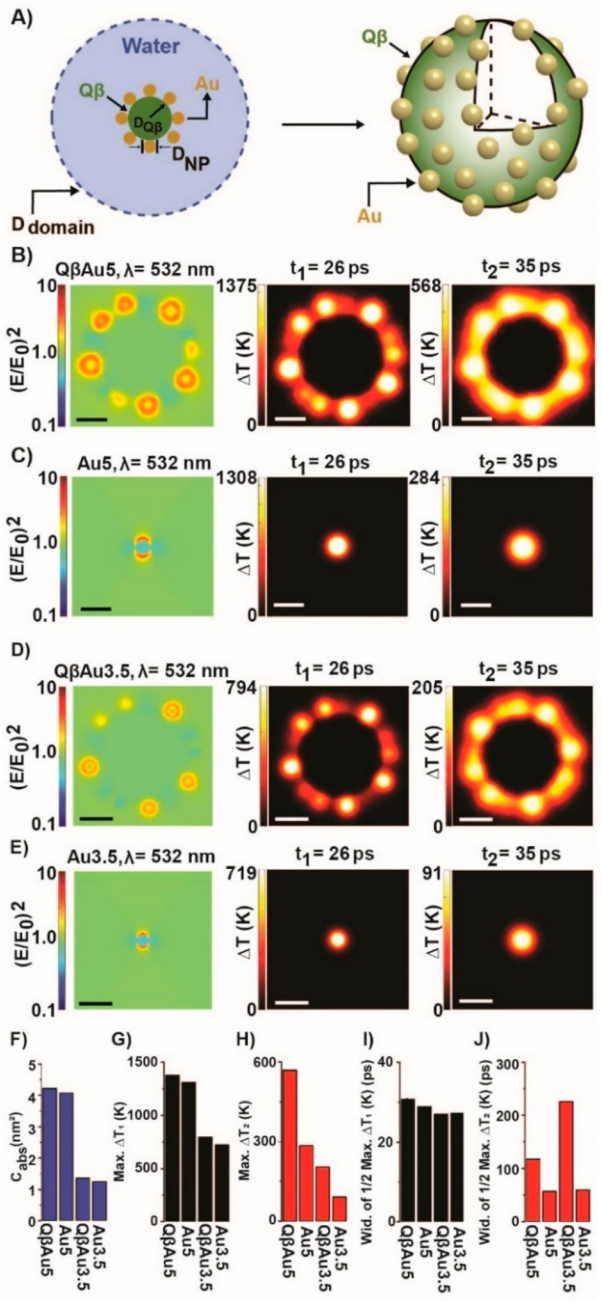

Figure 4. Temperature rise (ΔT) during the transient heating of individual AuNPs and conjugated QβAuNPs. (A) Schematic illustration of the model. The AuNPs are distributed in a Fibonacci lattice on the surface of the Qβ capsid, and the QβAuNPs are submerged in water. (B–E) Near-field enhancement ($(E/E_0)^2$) profile and temperature rise (ΔT) profile for QβAu5, Au5, QβAu3.5, and Au3.5. The scale bar represents 10 nm. The comparison of (F) C_{abs}, (G) maximum of ΔT_1, (H) maximum of ΔT_2, (I) the width of half-maximum ΔT_1, and (J) the width of half-maximum ΔT_2 for QβAu5, Au5, QβAu3.5, and Au3.5. Laser fluence for all cases is 34.8 mJ/cm^2.

temperature rise in AuNP (ΔT_1) increases rapidly to 1375 K for QβAu5 and 794 K for QβAu3.5. After the laser pulse, the AuNP cools gradually while the heat dissipates into the water domain and leads to heating overlap between AuNPs,[49] which is evidenced by an increasing temperature rise at the midpoint among AuNPs (ΔT_2). After the ΔT_2 reaches its peak value, it starts to cool down with further dissipation. Next, we compared the maximum of ΔT_1 and ΔT_2 for QβAuNPs and AuNP, respectively (Figure 4G,H). The maximum ΔT_1 for QβAuNP conjugation and individual AuNP are similar, whereas the maximum ΔT_2 for QβAuNP conjugation is significantly higher than that of individual AuNPs. Moreover, smaller AuNPs have a higher surface-volume ratio that can enhance heat dissipation and cooling. Importantly, for the same-sized AuNP, ΔT_2 for QβAuNPs conjugation is significantly higher than that of the single AuNP. This could be via the heating overlap between AuNPs in the conjugation, leading to a longer cooling time (Figure 4G). It should be noted that the mechanism of the nanobubble generation under the nanoscale is still unclear. Considering all these factors, the difference in the geometries of QβAuNPs and single AuNP, the size dependence of heating, the heating overlap at the midpoints between AuNPs, and a longer cooling time may all facilitate the nanobubble generation and lowered energy threshold for nanobubble detection with QβAuNP5 (Figure 3J).

CONCLUSION

In summary, immobilizing multiple size-controlled sub-10 nm AuNPs onto chemically modified thiol-rich virus-like particles provides a superior alternative to current state-of-the-art methodologies for plasmonically induced cavitation events. In this work, we exposed our scaffolds to high laser fluencies to elucidate the generation of PNBs and compared their photothermal properties to individual AuNPs. Our results demonstrated enhanced photothermal properties through the dramatic increase in PNB generation, lifetime, and probability at significantly lower laser fluencies than individual AuNPs, which required 7 times the laser energy to generate PNBs. Furthermore, we computationally studied the thermal transport of QβAuNP scaffolds and compared them with the individual AuNPs and found that these scaffolds induce delocalized heating among AuNPs, leading to more rapid heating and more gradual heat dissipation compared to individual AuNPs, correlating well with superior PNB formation at lower laser fluences. These results provide a promising outlook that can significantly contribute to applications in biomedicine, photothermal cancer therapies, and therapeutic drug delivery systems.

MATERIALS AND METHODS

Chemicals. The following chemicals were used: tryptone, yeast, sodium chloride, magnesium sulfate-anhydrous, potassium chloride, kanamycin, isopropyl β-D-1-thiogalactopyranoside (IPTG), potassium phosphate monobasic, potassium phosphate dibasic, ammonium sulfate, chloroform, butanol, sodium citrate tribasic, tannic acid, potassium carbonate, hydrogen tetrachloroaurate ($HAuCl_4 \cdot 3H_2O$), 2-(*N*-morpholino) ethanesulfonic acid (MES), 1-ethyl-3-(3-(dimethylamino)propyl) carbodiimide (EDC), *N*-hydroxysulfosuccinimide (Sulfo-NHS), 3-mercaptopropionic acid (MPA), Dulbecco's phosphate buffered saline (DPBS), Ellman's reagent, sodium phosphate dibasic, ethylenediaminetetraacetic acid (EDTA), sodium hydroxide, phosphoric acid, cysteine. Reagents were purchased from Sigma Life Science (Albuquerque, NM, USA), Research Products International (Mt Prospect, IL, USA), Thermo-Fisher Scientific (Waltham, MA, USA), Chem Impex Int'l (Wood Dale, IL, USA), AG Scientific (San Diego, CA, USA), BioWorld (Dublin, OH, USA), Acros Organics (New Jersey, NJ, USA), Caisson Laboratories (Smithfield, UT, USA), Aqua Solution (Deer Park, TX, USA), Alfa Aesar (Haverhill, MA, USA), Sigma-Aldrich (Saint-Louis, MO, USA).

https://doi.org/10.1021/acsnano.3c00638
ACS Nano XXXX, XXX, XXX−XXX

Qβ Production. 150 mL of a starter culture of *E. coli* BL21-DE3 cells with Qβ plasmid were amplified in 6 L of SOB media (50 μg·mL-1 Kanamycin) at 37 °C. Once an optimal O.D. between 0.4−0.7 was reached, induction of Qβ expression began with the addition of 1 mM IPTG and incubated at 37 °C overnight. Cells were centrifuged at 19,510 ×g for 30 min at 4 °C. The pellet was resuspended in 20−30 mL 0.1 M potassium phosphate (KP) buffer, pH 7.4. The cells were lysed using a Qsonica sonicator with 4 min cycles, 30 s on and off pulses, and 75% amplitude. The lysate was centrifuged at 19,510×*g* for 20 min at 4 °C. The pellet was discarded, and the supernatant was purified with ammonium sulfate (2 M final concentration) and incubated at 4 °C overnight. The suspension was centrifuged at 19,510×*g* for 20 min at 4 °C and resuspended in 20 mL 0.1 M KP buffer, pH 7.4. A chloroform-butanol extraction was performed with a 1:1 ratio of chloroform-butanol to 0.1 M KP buffer with dissolved protein and centrifuged at 19,510×*g* for 30 min at 4 °C. The top aqueous layer was extracted and layered onto sucrose gradients (10−40%). The sucrose gradient was ultracentrifuged for 16 h at 99,404×*g*. Qβ was pipetted from the sucrose gradients as a light blue band illuminated by a LED light and ultracentrifuged at 369,879×*g* for 2.5 h at 4 °C. A transparent pellet was found at the bottom of the tube. The supernatant was discarded, and the pellet was resuspended in 1−3 mL of 0.1 M KP buffer and characterized.

Thiolation of Qβ. The following solutions were prepared fresh in a stock of 100 mL MES buffer (100 mM, pH 5.5): 2.0 mL of EDC (1.0 M), 1.14 mL of MPA (50 mM) 250 μL of sulfo-NHS (1.0 M). Five μL of MPA was added into 1.14 mL MES buffer in an Eppendorf safe-lock-1.5 mL tube along with 28.5 μL EDC (1.0M) and 28.5 μL of sulfo-NHS (1.0 M). The solution was then vortexed and incubated in RT for 30 min. Then an additional 28.5 μL of EDC and sulfo-NHS were added to the solution. This mixture was then vortexed and incubated at rt for another 30 min. Once incubation was complete, 200 μL of DPBS (pH 7.4) was added to the mixture, along with 1.0 mg of Qβ (concentration was confirmed using Bradford Assay) and incubated at RT for 4.5−6 h. Once incubated, the solution was transferred into a 10−30 kDa cutoff Amicon-0.5 mL ultracentrifugal filter unit and centrifuged at 16,900 ×*g*, 10 min, 4 °C. The solution was then washed thoroughly with DPBS 4× (sufficient washing was confirmed using a working solution of Ellman's reagent and the disappearance of the yellow color after every wash). Concentration and conjugated free thiol were measured using Bradford assay and Ellman's Assay.

Ellman's Assay. The following procedure was used to perform an Ellman's Assay. An Ellman's reaction buffer was made by dissolving 1.20 g of sodium phosphate dibasic (Na_2HPO_4) and 37.2 mg of EDTA in 100 mL of Milli-Q water (0.1 M Na_2HPO_4, 1 mM EDTA). The pH was adjusted to 7.5−8 with solutions of sodium hydroxide (NaOH) or phosphoric acid (H_3PO_4). A cysteine working solution was made by dissolving 5.27 mg of cysteine in a 15 mL of reaction buffer (2 mM cysteine). The cysteine standards were made by serially diluting the cysteine working solution in reaction buffer with final concentrations of 2, 1, 0.5, 0.25, 0.125, 0.0625, and 0.03125 mM. Ellman's reagent is made by dissolving 4.0 mg Ellman's reagent in 1 mL of reaction buffer and vortexed for homogeneity. Lastly, the working solution was made by adding 125 μL of Ellman's reagent to 6.25 mL of reagent buffer. 7.5 μL of QβSH sample and standards were added to 96-well plates (n = 3) and 76.5 μL of Ellman's working reagent. They were mixed and incubated at rt for 15 min and analyzed on a plate reader (BioTeK Synergy H4 Hybrid Reader)) at 412 nm and calculated for the concentration of free thiols on Qβ (Figure S1). QβSH = 0.4113 mM.

Gold Nanoparticle Synthesis.[53,54] The following fresh stock solutions were prepared in Milli-Q water: 160 mL of sodium citrate tribasic (2.2 mM), 2.0 mL of tannic acid (2.5 mM and 5 mM), 10 mL of potassium carbonate (150 mM), and 10 mL of hydrogen tetrachloroaurate ($HAuCl_4{\cdot}3H_2O$) (25 mM). When measuring hydrogen tetrachloroaurate, a plastic spoon is recommended for the acidic nature of $HAuCl_4{\cdot}3H_2O$. A stock of $HAuCl_4{\cdot}3H_2O$ is viable in a 15 mL falcon tube for three months covered in aluminum foil at 4 °C. A solution of 150 mL of sodium citrate solution, 0.1 mL of tannic acid, and 1 mL of K_2CO_3 in a clean 250 mL flat bottom flask with a stirrer was heated in a water/oil bath to 70 °C (Figure S2A). $HAuCl_4$ solution (1 mL) was added swiftly to the flat bottom flask under vigorous vortex (>500 rpm), and stirring continued. Afterward, it was left to react for 5 min at 70 °C. The color changed from a gray/murky (Figure S2B) solution to an orange/red (Figure S2C) in 2 min or less. The solution was kept at 70 °C for 5 min further to ensure a complete reaction of the gold precursor (Figure S2D). Then the solution was cooled to rt, resulting in particles approximately 3.5 and 5 nm in size with a concentration of approximately 7×10^{13} NPs/mL (Figure S2E). The AuNP solution (150 mL) was transferred to a 10 kDa Amicon ultra-15 centrifugal filter unit and centrifuged at 3000 ×*g* for 10 min at 25 °C. The concentrated solution was collected. This process was repeated until a final volume of 1 mL of AuNPs was collected. Characterization was done by UV-vis (Figure S2F) and TEMs (Figure S2G).

AuNP Conjugation. Seventeen μL of QβSH (∼3−6 mg/mL), 233 μL of Milli-Q water, and 250 μL of concentrated AuNP were added into an Eppendorf safe-lock-1.5 mL tube and left to react for 12−15 h at rt. 2.2−10 mM of tribasic sodium citrate was dissolved in DPBS for the running buffer solution during the purification of QβAuNP composites from free AuNPs through a Sephadex G25 M column after incubation. Characterization was done by TEM (Figure S2H).

TEM. Micrographs of the QβAuNP composites were taken on a JEOL JEM-1400+ (JEOL, Tokyo, Japan) at 120 kV with a Gatan 4k × 4k CCD camera. Ten μL of the colloidal QβAuNP suspension was placed on a 300 mesh Forvar/carbon-coated copper grid (Electron Microscopy Sciences, Hatfield, PA, USA), allowed to stand for 1 min, and wicked off with Whatman#1 filter paper and allowed to air-dry completely. TEM micrographs of Qβ and QβSH were prepared using 5 μL of sample, placed onto grids, allowed to stand for 30 s, and wicked off with filter paper. An additional 5 μL of 2% uranyl acetate (SPI Supplies, West Chester, PA, USA) was placed on the grid, allowed to stand for 30 s, wicked off as before, and air-dried completely.

STEM. Sample preparation of QβAuNP composites followed the same process as in TEM micrographs. The morphology characterization of QβAuNPs (3.5 and 5 nm) was carried out via a Cs-corrected scanning transmission electron microscope (Cs-corrected STEM, JEOL ARM200F) operated at 200 kV. The acquisition semi-angle for high-angle annular dark-field detector was 90−370 mrad.

Nanobubble Detection for Individual AuNPs and QβAuNPs. Individual AuNPs (3.5 and 5 nm) and QβAuNPs (3.5 and 5 nm) were prepared with the same optical density and subsequently subjected to PNBs detection. Briefly, the sample solutions were flowed through a 400 μm borosilicate glass microcapillary (cat# 8240, VITROCOM) with a speed of 10 mL/min by a gastight glass syringe (cat# 81330, Hamilton). Then an ultrafast 532 nm picosecond pulse laser (green, 28 ps, 50 Hz) and a continuous 633 nm probe laser (red, CW) were simultaneously applied for generating and detecting of PNBs signals, respectively. The scattered signals from the as-generated PNBs were monitored by a fast-speed photodetector (FPD510-FV, MenloSystems) and collected by an oscilloscope (WAVESURFER 62MXS-B, TELEDYNE LECROY). Further signal analysis was processed using MATLAB script.

Computational Methodology. We first built a 3D boundary element model (BEM) and finite element model (FEM) to simulate the absorption cross-section (C_{abs}) and temperature rise (ΔT) during the plasmonic heating of QβAuNPs, respectively. The models are QβAuNPs that consist of a 30 nm protein core at the center and 46 AuNP with a diameter of 5 or 3.5 nm conjugated uniformly on the core (Figure 1A), and the QβAuNPs conjugation is immersed in aqueous solution. We assumed the AuNPs are evenly distributed on the surface of the Qβ protein and adopted a spherical Fibonacci lattice to avoid the polar effect.[55] The C_{abs} for QβAuNPs are listed in Table S1. For the FEM model, the size of the domain for the surrounding water (D_{domain}) is 300 nm. A boundary condition of constant temperature (T_{room} = 300 K) is set on the domain boundary. Here, we adopted the one temperature model since the electron cooling time

https://doi.org/10.1021/acsnano.3c00638
ACS Nano XXXX, XXX, XXX−XXX

for 5 nm AuNPs is around 10 ps, which is shorter than the time scale in our analysis (26 ps to 100 ns).[56] Since the mean free path in water is very small, we determined the temperature via Fourier's law, where the AuNPs are subjected to volumetric heating power and assumed no AuNP-water interfacial thermal resistance since it has a limited effect on the temperature in water.[57] The volumetric heating power (g, W/m^3) in the AuNP is determined as follows:

$$g = I \times C_{abs} \quad (1)$$

where I refers to laser fluence. For the single AuNP heating, the temperature is determined by analytical solution of heating.[58] The simulations were performed with COMSOL Multiphysics 5.4 and Matlab 2019b.

ASSOCIATED CONTENT

Supporting Information

The Supporting Information is available free of charge at https://pubs.acs.org/doi/10.1021/acsnano.3c00638.

Materials and methods, additional characterization, and figures (PDF)

AUTHOR INFORMATION

Corresponding Authors

Zhenpeng Qin − *Department of Mechanical Engineering, University of Texas at Dallas, Richardson, Texas 75080, United States;* orcid.org/0000-0003-3406-3045; Email: Zhenpeng.Qin@utdallas.edu

Jeremiah J. Gassensmith − *Department of Chemistry and Biochemistry and Department of Biomedical Engineering, University of Texas at Dallas, Richardson, Texas 75080, United States;* orcid.org/0000-0001-6400-8106; Email: Gassensmith@utdallas.edu

Authors

Perouza Parsamian − *Department of Chemistry and Biochemistry, University of Texas at Dallas, Richardson, Texas 75080, United States*

Yaning Liu − *Department of Mechanical Engineering, University of Texas at Dallas, Richardson, Texas 75080, United States;* orcid.org/0000-0001-8970-7245

Chen Xie − *Department of Mechanical Engineering, University of Texas at Dallas, Richardson, Texas 75080, United States*

Zhuo Chen − *Department of Chemistry and Biochemistry, University of Texas at Dallas, Richardson, Texas 75080, United States*

Peiyuan Kang − *Department of Mechanical Engineering, University of Texas at Dallas, Richardson, Texas 75080, United States;* orcid.org/0000-0003-1784-865X

Yalini H. Wijesundara − *Department of Chemistry and Biochemistry, University of Texas at Dallas, Richardson, Texas 75080, United States*

Noora M. Al-Kharji − *Department of Chemistry and Biochemistry, University of Texas at Dallas, Richardson, Texas 75080, United States*

Ryanne Nicole Ehrman − *Department of Chemistry and Biochemistry, University of Texas at Dallas, Richardson, Texas 75080, United States*

Orikeda Trashi − *Department of Chemistry and Biochemistry, University of Texas at Dallas, Richardson, Texas 75080, United States*

Jaona Randrianalisoa − *Institut de Thermique, Mécanique, Matériaux − ITheMM EA 7548 Université de Reims Champagne-Ardenne, F-51687 Reims, France*

Xiangyu Zhu − *Department of Materials Science and Engineering, University of Texas at Dallas, Richardson, Texas 75080, United States*

Matthew D'Souza − *Department of Chemistry and Biochemistry, University of Texas at Dallas, Richardson, Texas 75080, United States*

Lucas Anderson Wilson − *Department of Chemistry and Biochemistry, University of Texas at Dallas, Richardson, Texas 75080, United States*

Moon J. Kim − *Department of Materials Science and Engineering, University of Texas at Dallas, Richardson, Texas 75080, United States;* orcid.org/0000-0002-2972-493X

Complete contact information is available at: https://pubs.acs.org/10.1021/acsnano.3c00638

Author Contributions

P.P., Y.L., C.X., and Z.C. contributed equally (cofirst authors). Primary manuscript writing was done by P.P., Y.L., C.X., Z.C., J.J.G., and Z.Q. AuNP synthesis, bioconjugation, QβSH, and QβAuNP characterization were done by Z.C. and P.P. TEM micrographs were collected by Y.W. STEM micrographs were done by X.Z. and M.K., Qβ synthesis was done by P.P., N.M.A., R.N.E., O.T., M.B.D., and L.A.W. Nanobubble studies were done by Y.L. and K.P. Nanothermal transport computational studies were performed by Y.L., C.X., and J.R.

Notes

The authors declare no competing financial interest.

ACKNOWLEDGMENTS

We thank Dr. Jon Pokorski for providing us with *E. coli* BL21-DE3 cells. J.J.G. acknowledges support from the National Science Foundation (DMR-2003534) and the Welch Foundation (AT-1989-20190330).

ABBREVIATIONS

AuNP, gold nanoparticles; QβAuNP, Qβ gold nanoparticles; PNB, plasmonic nanobubble; C_{abs}, cross-section absorption

REFERENCES

(1) Bayda, S.; Adeel, M.; Tuccinardi, T.; Cordani, M.; Rizzolio, F., The History of Nanoscience and Nanotechnology: From Chemical-Physical Applications to Nanomedicine. *Molecules* **2020**, *25* (1).112

(2) Amendola, V.; Pilot, R.; Frasconi, M.; Marago, O. M.; Iati, M. A. Surface plasmon resonance in gold nanoparticles: a review. *J. Phys.: Condens. Matter* **2017**, *29* (20), 203002.

(3) Lashkari, S. M.; Kariminezhad, H.; Safarnezhad, N.; Amani, H. Surface plasmon resonance of naked gold nanoparticles for photodynamic inactivation of Escherichia coli. *Gold Bulletin* **2019**, *52* (1), 51−60.

(4) Su, Y.-H.; Ke, Y.-F.; Cai, S.-L.; Yao, Q.-Y. Surface plasmon resonance of layer-by-layer gold nanoparticles induced photoelectric current in environmentally-friendly plasmon-sensitized solar cell. *Light: Science & Applications* **2012**, *1* (6), e14−e14.

(5) Li, X.; Kang, P.; Chen, Z.; Lal, S.; Zhang, L.; Gassensmith, J. J.; Qin, Z. Rock the nucleus: significantly enhanced nuclear membrane permeability and gene transfection by plasmonic nanobubble induced nanomechanical transduction. *Chem. Commun.* **2018**, *54* (20), 2479−2482.

(6) Huang, X.; El-Sayed, M. A. Gold nanoparticles: Optical properties and implementations in cancer diagnosis and photothermal therapy. *Journal of Advanced Research* **2010**, *1* (1), 13−28.

(7) Kim, H. S.; Lee, D. Y. Near-Infrared-Responsive Cancer Photothermal and Photodynamic Therapy Using Gold Nanoparticles. *Polymers (Basel)* **2018**, *10* (9), 961.

(8) Rozanova, N.; Zhang, J. Photothermal ablation therapy for cancer based on metal nanostructures. *Science in China Series B: Chemistry* **2009**, *52* (10), 1559−1575.
(9) Wagner, D. S.; Delk, N. A.; Lukianova-Hleb, E. Y.; Hafner, J. H.; Farach-Carson, M. C.; Lapotko, D. O. The in vivo performance of plasmonic nanobubbles as cell theranostic agents in zebrafish hosting prostate cancer xenografts. *Biomaterials* **2010**, *31* (29), 7567−74.
(10) Kang, P.; Chen, Z.; Nielsen, S. O.; Hoyt, K.; D'Arcy, S.; Gassensmith, J. J.; Qin, Z. Molecular Hyperthermia: Spatiotemporal Protein Unfolding and Inactivation by Nanosecond Plasmonic Heating. *Small* **2017**, *13* (36), 1700841.
(11) Qin, Z.; Bischof, J. C. Thermophysical and biological responses of gold nanoparticle laser heating. *Chem. Soc. Rev.* **2012**, *41* (3), 1191−217.
(12) Li, X.; Vemireddy, V.; Cai, Q.; Xiong, H.; Kang, P.; Li, X.; Giannotta, M.; Hayenga, H. N.; Pan, E.; Sirsi, S. R.; Mateo, C.; Kleinfeld, D.; Greene, C.; Campbell, M.; Dejana, E.; Bachoo, R.; Qin, Z. Reversibly Modulating the Blood-Brain Barrier by Laser Stimulation of Molecular-Targeted Nanoparticles. *Nano Lett.* **2021**, *21* (22), 9805−9815.
(13) Li, X.; Cai, Q.; Wilson, B. A.; Fan, H.; Giannotta, M.; Bachoo, R.; Qin, Z., Calcium-Mediated Modulation of Blood-Brain Barrier Permeability by Laser Stimulation of Endothelial-Targeted Nanoparticles. *bioRxiv*, 2022.06.02.494541, ver. 1, 2022. https://www.biorxiv.org/content/10.1101/2022.06.02.494541v1 (accessed 2023-02-27).
(14) Bromley, K. M.; Patil, A. J.; Perriman, A. W.; Stubbs, G.; Mann, S. Preparation of high quality nanowires by tobacco mosaic virus templating of gold nanoparticles. *J. Mater. Chem.* **2008**, *18* (40), 4796.
(15) Fernandes, R.; Li, M.; Dujardin, E.; Mann, S.; Kanaras, A. G. Ligand-mediated self-assembly of polymer-enveloped gold nanoparticle chains and networks. *Chem. Commun.* **2010**, *46* (40), 7602−7604.
(16) Mann, S. Self-assembly and transformation of hybrid nano-objects and nanostructures under equilibrium and non-equilibrium conditions. *Nature materials* **2009**, *8* (10), 781−792.
(17) Shenton, W.; Davis, S. A.; Mann, S. Directed Self-Assembly of Nanoparticles into Macroscopic Materials Using Antibody−Antigen Recognition. *Adv. Mater.* **1999**, *11* (6), 449−452.
(18) Zhou, K.; Zhang, J.; Wang, Q. Site-selective nucleation and controlled growth of gold nanostructures in tobacco mosaic virus nanotubulars. *Small* **2015**, *11* (21), 2505−2509.
(19) Li, F.; Wang, Q. Fabrication of nanoarchitectures templated by virus-based nanoparticles: strategies and applications. *Small* **2014**, *10* (2), 230−245.
(20) Lukianova-Hleb, E.; Hu, Y.; Latterini, L.; Tarpani, L.; Lee, S.; Drezek, R. A.; Hafner, J. H.; Lapotko, D. O. Plasmonic Nanobubbles as Transient Vapor Nanobubbles Generated around Plasmonic Nanoparticles. *ACS Nano* **2010**, *4* (4), 2109−2123.
(21) Lukianova-Hleb, E. Y.; Hanna, E. Y.; Hafner, J. H.; Lapotko, D. O. Tunable plasmonic nanobubbles for cell theranostics. *Nanotechnology* **2010**, *21* (8), 085102.
(22) Lukianova-Hleb, E. Y.; Kim, Y.-S.; Belatsarkouski, I.; Gillenwater, A. M.; O'Neill, B. E.; Lapotko, D. O. Intraoperative diagnostics and elimination of residual microtumours with plasmonic nanobubbles. *Nat. Nanotechnol.* **2016**, *11* (6), 525−532.
(23) Lukianova-Hleb, E. Y.; Koneva, II; Oginsky, A. O.; La Francesca, S.; Lapotko, D. O. Selective and self-guided micro-ablation of tissue with plasmonic nanobubbles. *J. Surg Res.* **2011**, *166* (1), e3−13.
(24) Lukianova-Hleb, E. Y.; Ren, X.; Sawant, R. R.; Wu, X.; Torchilin, V. P.; Lapotko, D. O. On-demand intracellular amplification of chemoradiation with cancer-specific plasmonic nanobubbles. *Nature Medicine* **2014**, *20* (7), 778−784.
(25) Lukianova-Hleb, E. Y.; Ren, X.; Townley, D.; Wu, X.; Kupferman, M. E.; Lapotko, D. O. Plasmonic nanobubbles rapidly detect and destroy drug-resistant tumors. *Theranostics* **2012**, *2* (10), 976−87.
(26) Lukianova-Hleb, E. Y.; Volkov, A. N.; Lapotko, D. O. Laser Pulse Duration Is Critical For the Generation of Plasmonic Nanobubbles. *Langmuir* **2014**, *30* (25), 7425−7434.
(27) Kitz, M.; Preisser, S.; Wetterwald, A.; Jaeger, M.; Thalmann, G. N.; Frenz, M. Vapor bubble generation around gold nano-particles and its application to damaging of cells. *Biomed. Opt. Express* **2011**, *2* (2), 291−304.
(28) Danysh, B. P.; Constantinou, P. E.; Lukianova-Hleb, E. Y.; Lapotko, D. O.; Carson, D. D. The MUC1 Ectodomain: A Novel and Efficient Target for Gold Nanoparticle Clustering and Vapor Nanobubble Generation. *Theranostics* **2012**, *2* (8), 777−87.
(29) Lukianova-Hleb, E. Y.; Ren, X.; Zasadzinski, J. A.; Wu, X.; Lapotko, D. O. Plasmonic nanobubbles enhance efficacy and selectivity of chemotherapy against drug-resistant cancer cells. *Adv. Mater.* **2012**, *24* (28), 3831−7.
(30) Shahrivarkevishahi, A.; Hagge, L. M.; Brohlin, O. R.; Kumari, S.; Ehrman, R.; Benjamin, C.; Gassensmith, J. J. Virus-like particles: a self-assembled toolbox for cancer therapy. *Mater. Today Chem.* **2022**, *24*, 100808.
(31) Chen, Z.; Li, N.; Li, S.; Dharmarwardana, M.; Schlimme, A.; Gassensmith, J. J. Viral chemistry: the chemical functionalization of viral architectures to create new technology. *Wiley Interdiscip Rev. Nanomed Nanobiotechnol* **2016**, *8* (4), 512−34.
(32) Rohovie, M. J.; Nagasawa, M.; Swartz, J. R. Virus-like particles: Next-generation nanoparticles for targeted therapeutic delivery. *Bioeng Transl Med.* **2017**, *2* (1), 43−57.
(33) Lumata, J. L.; Ball, D.; Shahrivarkevishahi, A.; Luzuriaga, M. A.; Herbert, F. C.; Brohlin, O.; Lee, H.; Hagge, L. M.; D'Arcy, S.; Gassensmith, J. J. Identification and physical characterization of a spontaneous mutation of the tobacco mosaic virus in the laboratory environment. *Sci. Rep* **2021**, *11* (1), 15109.
(34) Li, S.; Gassensmith, J. J. Synthesis of Metal-Organic Frameworks on Tobacco Mosaic Virus Templates. *Methods Mol. Biol.* **2018**, *1798*, 95−108.
(35) Luzuriaga, M. A.; Welch, R. P.; Dharmarwardana, M.; Benjamin, C. E.; Li, S.; Shahrivarkevishahi, A.; Popal, S.; Tuong, L. H.; Creswell, C. T.; Gassensmith, J. J. Enhanced Stability and Controlled Delivery of MOF-Encapsulated Vaccines and Their Immunogenic Response In Vivo. *ACS Appl. Mater. Interfaces* **2019**, *11* (10), 9740−9746.
(36) Herbert, F. C.; Brohlin, O. R.; Galbraith, T.; Benjamin, C.; Reyes, C. A.; Luzuriaga, M. A.; Shahrivarkevishahi, A.; Gassensmith, J. J. Supramolecular Encapsulation of Small-Ultrared Fluorescent Proteins in Virus-Like Nanoparticles for Noninvasive In Vivo Imaging Agents. *Bioconjug Chem.* **2020**, *31* (5), 1529−1536.
(37) Shahrivarkevishahi, A.; Luzuriaga, M. A.; Herbert, F. C.; Tumac, A. C.; Brohlin, O. R.; Wijesundara, Y. H.; Adlooru, A. V.; Benjamin, C.; Lee, H.; Parsamian, P.; Gadhvi, J.; De Nisco, N. J.; Gassensmith, J. J. PhotothermalPhage: A Virus-Based Photothermal Therapeutic Agent. *J. Am. Chem. Soc.* **2021**, *143* (40), 16428−16438.
(38) Benjamin, C. E.; Chen, Z.; Kang, P.; Wilson, B. A.; Li, N.; Nielsen, S. O.; Qin, Z.; Gassensmith, J. J. Site-Selective Nucleation and Size Control of Gold Nanoparticle Photothermal Antennae on the Pore Structures of a Virus. *J. Am. Chem. Soc.* **2018**, *140* (49), 17226−17233.
(39) Golmohammadi, R.; Fridborg, K.; Bundule, M.; Valegård, K.; Liljas, L. The crystal structure of bacteriophage Qβ at 3.5 å resolution. *Structure* **1996**, *4* (5), 543−554.
(40) Banerjee, D.; Liu, A. P.; Voss, N. R.; Schmid, S. L.; Finn, M. G. Multivalent display and receptor-mediated endocytosis of transferrin on virus-like particles. *Chembiochem* **2010**, *11* (9), 1273−1279.
(41) Rhee, J.-K.; Hovlid, M.; Fiedler, J. D.; Brown, S. D.; Manzenrieder, F.; Kitagishi, H.; Nycholat, C.; Paulson, J. C.; Finn, M. G. Colorful virus-like particles: fluorescent protein packaging by the Qβ capsid. *Biomacromolecules* **2011**, *12* (11), 3977−3981.
(42) Pokorski, J. K.; Hovlid, M. L.; Finn, M. G. Cell Targeting with Hybrid Qβ Virus-Like Particles Displaying Epidermal Growth Factor. *Chembiochem* **2011**, *12* (16), 2441−2447.

https://doi.org/10.1021/acsnano.3c00638
ACS Nano XXXX, XXX, XXX−XXX

(43) Chen, Z.; Boyd, S. D.; Calvo, J. S.; Murray, K. W.; Mejia, G. L.; Benjamin, C. E.; Welch, R. P.; Winkler, D. D.; Meloni, G.; D'Arcy, S.; Gassensmith, J. J. Fluorescent Functionalization across Quaternary Structure in a Virus-like Particle. *Bioconjugate Chem.* **2017**, *28* (9), 2277−2283.
(44) Lee, H.; Benjamin, C. E.; Nowak, C. M.; Tuong, L. H.; Welch, R. P.; Chen, Z.; Dharmarwardana, M.; Murray, K. W.; Bleris, L.; D'Arcy, S.; Gassensmith, J. J. Regulating the Uptake of Viral Nanoparticles in Macrophage and Cancer Cells via a pH Switch. *Mol. Pharmaceutics* **2018**, *15* (8), 2984−2990.
(45) Benjamin, C. E.; Chen, Z.; Brohlin, O. R.; Lee, H.; Shahrivarkevishahi, A.; Boyd, S.; Winkler, D. D.; Gassensmith, J. J. Using FRET to measure the time it takes for a cell to destroy a virus. *Nanoscale* **2020**, *12* (16), 9124−9132.
(46) Benjamin, C.; Brohlin, O.; Shahrivarkevishahi, A.; Gassensmith, J. J. Virus like particles: fundamental concepts, biological interactions, and clinical applications. In *Nanoparticles for Biomedical Applications*; Chung, E. J., Leon, L., Rinaldi, C., Eds.; Elsevier, 2020; pp 153−174.
(47) Lee, H.; Shahrivarkevishahi, A.; Lumata, J. L.; Luzuriaga, M. A.; Hagge, L. M.; Benjamin, C. E.; Brohlin, O. R.; Parish, C. R.; Firouzi, H. R.; Nielsen, S. O.; Lumata, L. L.; Gassensmith, J. J. Supramolecular and biomacromolecular enhancement of metal-free magnetic resonance imaging contrast agents. *Chemical Science* **2020**, *11* (8), 2045−2050.
(48) Wijesundara, Y. H.; Herbert, F. C.; Kumari, S.; Howlett, T.; Koirala, S.; Trashi, O.; Trashi, I.; Al-Kharji, N. M.; Gassensmith, J. J. Rip it, stitch it, click it: A Chemist's guide to VLP manipulation. *Virology* **2022**, *577*, 105−123.
(49) Xie, C.; Qin, Z. Spatiotemporal Evolution of Temperature During Transient Heating of Nanoparticle Arrays. *Journal of heat transfer* **2022**, *144*, 031204.
(50) Ogunyankin, M. O.; Shin, J. E.; Lapotko, D. O.; Ferry, V. E.; Zasadzinski, J. A. Optimizing the NIR Fluence Threshold for Nanobubble Generation by Controlled Synthesis of 10−40 nm Hollow Gold Nanoshells. *Adv. Funct. Mater.* **2018**, *28* (10), 1705272.
(51) Vines, J. B.; Yoon, J.-H.; Ryu, N.-E.; Lim, D.-J.; Park, H. Gold Nanoparticles for Photothermal Cancer Therapy. *Frontiers in chemistry* **2019**, *7*, 167−167.
(52) Kennedy, L. C.; Bickford, L. R.; Lewinski, N. A.; Coughlin, A. J.; Hu, Y.; Day, E. S.; West, J. L.; Drezek, R. A. A New Era for Cancer Treatment: Gold-Nanoparticle-Mediated Thermal Therapies. *Small (Weinheim an der Bergstrasse, Germany)* **2011**, *7* (2), 169−183.
(53) Piella, J.; Bastús, N. G.; Puntes, V. Size-Controlled Synthesis of Sub-10-nanometer Citrate-Stabilized Gold Nanoparticles and Related Optical Properties. *Chem. Mater.* **2016**, *28* (4), 1066−1075.
(54) Qin, Z.; Wang, Y.; Randrianalisoa, J.; Raeesi, V.; Chan, W. C. W.; Lipiński, W.; Bischof, J. C. Quantitative Comparison of Photothermal Heat Generation between Gold Nanospheres and Nanorods. *Sci. Rep.* **2016**, *6*, 29836.
(55) González, Á. Measurement of Areas on a Sphere Using Fibonacci and Latitude−Longitude Lattices. *Mathematical Geosciences* **2010**, *42* (1), 49−64.
(56) Nguyen, S. C.; Zhang, Q.; Manthiram, K.; Ye, X.; Lomont, J. P.; Harris, C. B.; Weller, H.; Alivisatos, A. P. Study of Heat Transfer Dynamics from Gold Nanorods to the Environment via Time-Resolved Infrared Spectroscopy. *ACS Nano* **2016**, *10* (2), 2144−2151.
(57) Kang, P.; Xie, C.; Fall, O.; Randrianalisoa, J.; Qin, Z. Computational Investigation of Protein Photoinactivation by Molecular Hyperthermia. *Journal of Biomechanical Engineering* **2021**, *143* (3), 031004 DOI: 10.1115/1.4049017.
(58) Fasla, B.; Senoudi, A. R.; Boussaid, A.; Benmouna, M.; Benmouna, R. Heating of Biological Tissues by Gold Nano Particles: Effects of Particle Size and Distribution. *Journal of Biomaterials and Nanobiotechnology* **2011**, *02*, 49−54.

https://doi.org/10.1021/acsnano.3c00638
ACS Nano XXXX, XXX, XXX−XXX